Article

Expediting Corrosion Engineering for Sulfur-Doped, Self-Supporting Ni-Fe Layered Dihydroxide in Efficient Aqueous Oxygen Evolution

Yingjun Ma [1,2], Jie Wang [1,2,3,]*, Hangning Liu [2], Lin Wang [2], Changhui Sun [2], Liangyu Gong [2], Xiaogang Zhang [1,]* and Jiefang Zhu [3,]*

[1] Jiangsu Key Laboratory of Electrochemical Energy Storage Technology, College of Material Science and Engineering, Nanjing University of Aeronautics and Astronautics, Nanjing 210016, China; myj3752@163.com

[2] Qingdao Engineering Research Center of Agricultural Recycling Economy Materials, College of Chemistry and Pharmaceutical Sciences, Qingdao Agricultural University, Qingdao 266109, China; 20200201033@stu.qau.edu.cn (H.L.); wlinlin990304@163.com (L.W.); sunchanghui123@stu.qau.edu.cn (C.S.); lygong@163.com (L.G.)

[3] Department of Chemistry, Ångström Laboratory, Uppsala University, 75121 Uppsala, Sweden

* Correspondence: wangjie@qau.edu.cn (J.W.); azhangxg@nuaa.edu.cn (X.Z.); jiefang.zhu@kemi.uu.se (J.Z.)

Abstract: Electrochemical water-splitting is widely acknowledged as a renewable strategy for hydrogen production, but it is primarily constrained by the sluggish reaction kinetics of the anode oxygen evolution reaction (OER). In our study, we employ a fast room-temperature corrosion engineering strategy for the construction of a sulfur-doped Ni-Fe layered dihydroxide catalyst (S-NiFe LDH). With the assistance of a sulfur source, microsphere morphology with an ultra-thin lamellar surface cross-arrangement can be rapidly grown on the surface of an iron foam substrate, ensuring a substantial electrochemical interface. The composition of Ni species in the catalysts can be regulated by simply adjusting the amount of Ni^{2+} and reaction time. Functioning as an OER catalyst, the S-NiFe LDH demonstrates high activity and reaction kinetics, featuring a minimal overpotential of 120.0 mV to deliver a current density of 10 mA cm^{-2}, a small Tafel slope of 39.5 mV dec^{-1} and a notable electrical double-layer capacitance (C_{dl}) of 31.3 mF cm^{-2}. The remarkable electrocatalytic performance can be attributed to its distinctive three-dimensional (3D) structure and sulfur dopants, which effectively regulate the electrochemical interface and electronic structure of NiFe LDH. This work provides valuable insights for expeditious materials design.

Keywords: corrosion engineering; NiFe LDH; S-doping; oxygen evolution reaction; reaction kinetics

1. Introduction

The excessive consumption of fossil fuels has precipitated severe environmental crises and energy shortages [1,2]. In response, renewable energy resources have garnered widespread attention, with hydrogen emerging as a promising alternative. When hydrogen reacts with oxygen, it produces water, making it a clean energy option. However, the conventional method of obtaining hydrogen through the steam reforming process is energy-intensive and often results in a carbon monoxide byproduct. This limitation restricts its further application and favors the use of renewable energy devices instead. As an alternative, electrocatalytic water decomposition has become a pivotal technology for hydrogen and oxygen production. Unlike the steam reforming process, which demands a high energy input, electrocatalytic decomposition offers a more moderate approach. Yet, initiating water electrolysis through this method requires a voltage exceeding 1.23 V due to the sluggish kinetics of the reaction, resulting in substantial polarization [3–5]. Compared to the hydrogen evolution reaction (HER) at the cathode, the oxygen evolution reaction (OER) at the anode plays a crucial role, particularly because it involves multi-step electron

transfers [6–13]. To facilitate this process, highly efficient electrocatalysts are essential to lower the energy barrier for breaking the O-H bond and forming the O-O bond [14]. Given the practical implications and feasibility of these advancements, reducing energy consumption and processing time have emerged as key objectives in the water-splitting industry [15–18].

At present, RuO_2, IrO_2 and other noble metal catalysts are commonly recognized to be commercially used in electrochemical water-splitting applications, but their scarcity and high price presented an obstacle to scale-up [19–23]. Comparatively, a large number of non-noble-metal-based catalysts, especially transition metal sulfides [24–26] phosphates [27], nitrides [28–30] and hydroxide [31,32], have been extensively studied due to their abundant earth reserves, low price and tunable electronic structure. Considering that the price of Fe is a hundred times lower than that of Ni and Co, the combination of Fe with other metal species for the construction of binary and ternary catalysts has been widely investigated [33–39]. Typically, Ni-Fe layered dihydroxide (NiFe LDH) is considered as an effective alternative material for noble metal catalysts because of its unique electronic properties. Moreover, the electronic structure and electrochemical interfaces can be further regulated by optimizing the ionic components. Typically, corrosion has been considered as a mild and controllable top-down strategy for the construction of NiFe LDH with a specific structure. For example, Li et al. have adopted the corrosion strategy to convert substrates into highly active and stable OER catalysts under ambient pressure. The electronic structure and chemical kinetics of the catalyst were improved by controlling the metal content and element doping [40]. Fu et al. reported a porous NiFe LDH catalyst with rich edge/surface-Fe defects on a nickel foam substrate via an elaborate atmosphere corrosion strategy. The Fe defects were derived from the local unequal-stoichiometric ratio of Fe/Ni in the nanometer or sub-nanometer region, which could be regulated by two aspects: (i) the unbalanced permeating of the acid vapor; (ii) the confined reaction of local Fe and Ni species ionized by the acid vapor. Also benefiting from the abundant defects, NiFe LDH demonstrated superior OER performance relative to the catalyst synthesized via conventional process. It should be noted that the atmosphere corrosion strategy is green and economic, which is suitable for large-scale applications [41]. Accordingly, to further enhance the OER properties of NiFe LDH, heteroatom doping would be a potential method, but there are still few reports related to the anion doping.

In this study, we have introduced a rapid room-temperature corrosion engineering approach to fabricate a sulfur-doped NiFe LDH catalyst (S-NiFe LDH) using iron foam (IF) as the substrate. The resulting catalyst exhibits a unique cross-arrangement of ultra-thin lamellar microstructures self-assembling into three-dimensional (3D) microspheres. This distinctive morphology is advantageous as it is beneficial for enlarging the electrochemical interfaces, crucial for efficient catalytic performance. The composition of Ni species within the NiFe LDH structure was easily modulated by adjusting the amount of Ni^{2+} ions and the reaction time during synthesis. The incorporation of sulfur sources in the synthesis process played three crucial roles: (i) promoting the surface corrosion rate on IF substrate; (ii) accelerating the formation of NiFe LDH; (iii) resulting in S dopants in the NiFe LDH structure. Therefore, the S-NiFe LDH with optimized electronic structure and morphology improved the OER performance, especially the reaction activities, reaction kinetics and long-term durability. This work offers valuable insights into the fabrication of anion-doped catalysts using a rapid corrosion strategy, presenting a promising catalyst for electrocatalytic applications.

2. Results and Discussion

2.1. Structural Characterization

As demonstrated from the catalyst construction schematic in Figure 1, a spontaneous corrosion engineering strategy was adopted to construct a S-NiFe LDH catalyst in the natural dissolved oxygen environment for the electrocatalytic OER application. During the synthetic process, the IF served as both a skeleton and Fe source, which are beneficial

for accelerating electron transfer and providing a large corrosion interface. In detail, the IF is first corroded via oxygen corrosion (Equations (1) and (2)), in which the oxygen comes from the air dissolved in the solution. The slight reducibility of $S_2O_3^{2-}$ in the solution will assist in stabilizing the metal ions at the IF surface. Subsequently, the corroded Fe ions combine with free sulfur species$^-$, Ni^{2+}, and OH^- to form S-NiFe LDH. The corrosion process is as follows:

$$\text{Anode reaction: } Fe \leftrightarrow Fe^{2+} + 2e^-, Fe^{2+} \leftrightarrow Fe^{3+} + e^- \tag{1}$$

$$\text{Cathode reaction: } O_2 + 2H_2O + 4e^- \leftrightarrow 4OH^- \tag{2}$$

$$\text{Precipitation reaction: } Fe^{3+} + Ni^{2+} + xOH^- + xS^{2-} \leftrightarrow xS\text{-}NiFe(OH)_x \tag{3}$$
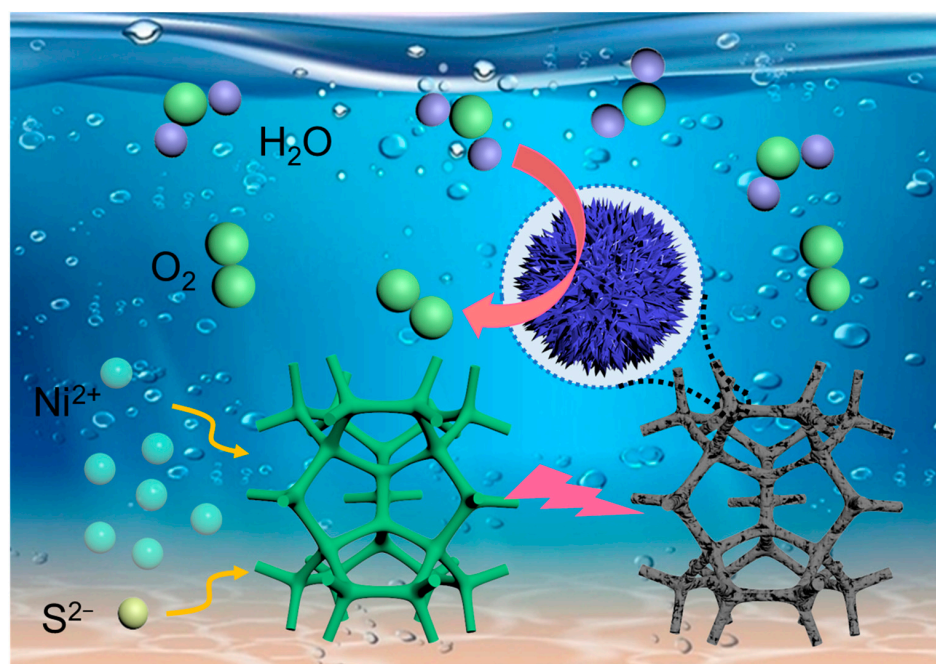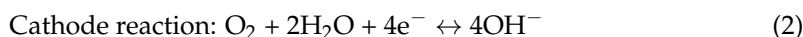

Figure 1. Schematic illustration for the preparation of the S-NiFe LDH electrode and its application in the electrochemical water-splitting process.

During the corrosion process, different corrosion products were obtained by tuning the Ni^{2+} concentrations (Table S1). X-ray diffraction (XRD) was performed to characterize the phase information of the corrosion products. As shown in Figure 2a, the XRD pattern of S-NiFe LDH reacted at different Ni^{2+} concentrations showed two crystalline phases, in which the diffraction peaks at 44.6°, 65.1° and 82.3° correspond to the crystalline phases of Fe (PDF card: 06-0696) and the diffraction peaks at 11.5°, 23.3° and 34.6° correspond to the NiFe LDH phase (PDF card: 51-0463). It should be noted that there is negligible crystal information associated with S species, indicating that the S component in the products may exist as amorphous S species or that trace amounts of S species remained after the reaction.

The morphology and microstructure of the as-prepared S-NiFe LDH were meticulously characterized using advanced techniques including scanning electron microscopy (SEM), transmission electron microscopy (TEM) and energy-dispersive spectroscopy (EDS). The resulting analysis unveiled intriguing details about the structure of the catalyst. As shown in Figure 2b,c, SEM images depicted the presence of three-dimensional (3D) structured microspheres prominently growing on the surface of the IF substrate. These microspheres exhibit a well-organized arrangement of ultra-thin lamellae, with a measured lamellar thickness of approximately 10 nm as determined from the enlarged SEM image of the S-NiFe LDH. The 3D structure is composed of a well-cross-arranged ultra-thin lamellar structure, which is conducive to increasing the contact area between the electrolyte and catalyst, which is essential for improving the utilization of active sites within the catalyst

material, thereby boosting its efficiency in catalytic reactions. Furthermore, the TEM image in Figure 2d provides additional insights into the nanosheet morphology of the S-NiFe LDH. The nanosheets appear somewhat randomly distributed, likely due to the vigorous ultrasonic dispersion with ethanol solvent before the TEM operation. Upon closer inspection at higher magnification (Figure 2e), distinct lattice fringes become apparent, indicating the excellent crystal structure of the S-NiFe LDH catalyst. Moreover, the width of two adjacent fringes was measured to be 0.26 nm, corresponding to the (0 1 2) crystal plane of the S-NiFe LDH. To further confirm the elemental composition and distribution within the S-NiFe LDH, EDS characterization of a selected sample was performed as shown in Figures 2f and S1. The EDS analysis demonstrated a uniform distribution of Ni, Fe, O and S species throughout the sample. Notably, the atomic percentage of S was found to be 4.2% (as shown in Table S2), indicating the successful doping of sulfur in the S-NiFe LDH structure. This sulfur doping is significant as it may optimize the electronic properties of the NiFe LDH and enhance the catalytic performance.
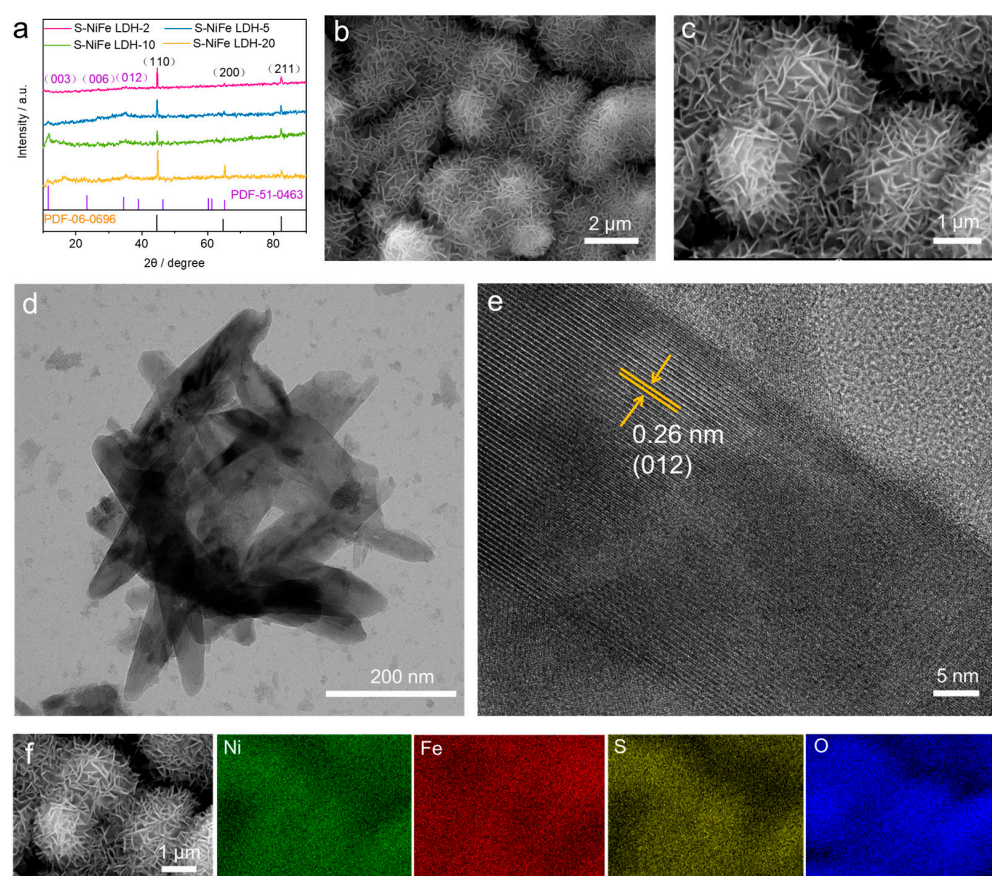

Figure 2. (**a**) XRD pattern of S-NiFe LDH reacted at different Ni^{2+} concentrations; (**b**) SEM image and enlarged magnification SEM image (**c**) of S-NiFe LDH; (**d**) TEM image of S-NiFe LDH; (**e**) high-resolution TEM (HRTEM) image of S-NiFe LDH; (**f**) SEM image of S-NiFe LDH and corresponding EDS maps of Fe, O and S.

Additionally, the effects of Ni^{2+} concentration and reaction time for the structure regulation of S-NiFe LDH were investigated in detail. When the amount of Ni^{2+} was tuned to 2 mmol, the surface of the IF formed a corrosion product that features a lamellar cross-arranged sphere morphology, but the boundary between spheres was difficult to clarify (Figure 3a). When the amount of Ni^{2+} was increased to 5 mmol, the lamellar structure gradually coalesced (Figure 3b), and the boundary between the spheres became much clearer. When the amount of Ni^{2+} was increased to 10 mmol, the 3D microsphere structure could be seen obviously (Figure 3c). Excessive Ni^{2+} concentration (20 mmol) resulted in

severe destruction of the sphere structure (Figure 3d). Accordingly, the S-NiFe LDH-2, S-NiFe LDH-5, S-NiFe LDH-10 and S-NiFe LDH-20 have an average lamellar thickness of 161.3 nm, 80.0 nm, 58.8 nm and 60.1 nm, respectively. Therefore, with the increase in the Ni^{2+} ratio, the thickness of the lamellar thickness decreases first and then increases, demonstrating that the Ni^{2+} ratio plays an important role in regulating the thickness of the lamellar structure. The same phenomenon was also found when gradually increasing the reaction time. At the reaction time of 2 h, microspheres began to form (Figure S2a). The diameter of the microspheres gradually increased as the reaction time extended from 2 h to 6 h (Figure S2b,c). After a 6 h reaction, the spheres began to aggregate (Figure S2d) and even collapse (Figure S2e). The results demonstrated that the Ni^{2+} concentration of 10 mmol and reaction time of 6 h would result in a sphere structure with a large size and lamellar micromorphology.
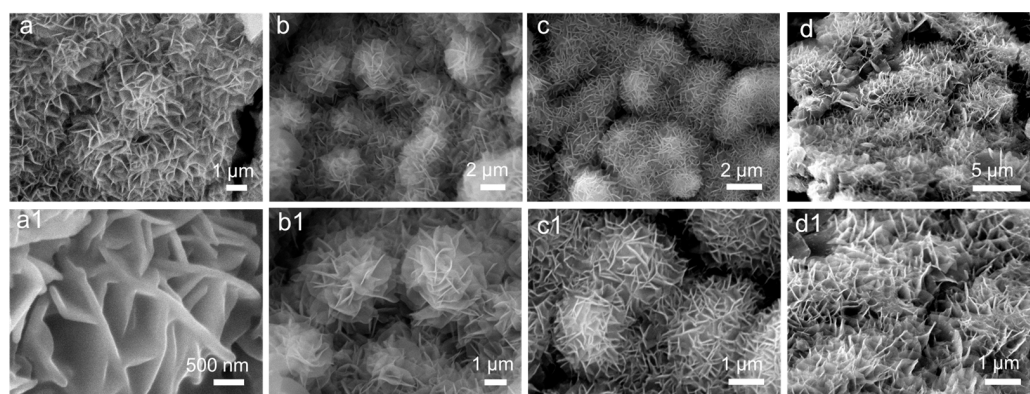

Figure 3. SEM image and enlarged magnification SEM image of S-NiFe LDH-2 (**a**,**a1**); SEM image and enlarged magnification SEM image of S-NiFe LDH-5 (**b**,**b1**); SEM image and enlarged magnification SEM image of S-NiFe LDH-10 (**c**,**c1**); SEM image and enlarged magnification SEM image of S-NiFe LDH-20 (**d**,**d1**).

The surface information of NiFe LDH obtained at different Ni^{2+} concentrations was characterized by the XPS technique. As shown from the full-range XPS spectra in Figure 4a, the binding energies located at near 162.5, 286.7, 530.0, 855.0 and 712.5 eV correspond to S 2p, C 1s, O 1s, Ni 2p and Fe 2p, respectively. The atomic S percentages in S-NiFe LDH-2, S-NiFe LDH-5, S-NiFe LDH-10 and S-NiFe LDH-20 were 3.7%, 5.0%, 3.9% and 4.0%. The sulfur content showed a volcanic trend with the increasing concentration of Ni^{2+}, which may be ascribed to the morphology evolution and change in the Ni/Fe ratio. The presence of the C 1s signal can be attributed to the use of a conductive binder which was applied to fix the sample before XPS measurements. To further investigate the valence state of the samples, high-resolution XPS spectra were obtained. As shown in Figure 4b, the high-resolution XPS spectra showed typical peaks at 855.05 eV corresponding to the $2p_{3/2}$ binding energies of Ni 2p, demonstrating the existing valence of Ni^{2+}. Peaks located at 861.3 eV corresponded to the satellite oscillation peaks of Ni 2p [42,43]. In addition, the S-NiFe LDH-2 sample showed a Ni^0 peak at a binding energy of 854.9 eV, which may be due to the existence of a displacement reaction between IF and Ni^{2+}. The Fe 2p spectrum (Figure 4c) was deconvoluted into six peaks, in which peaks at binding energies of 710.7 and 724.1 eV represent Fe^{2+}, peaks at 713.5 and 725.1 eV represent Fe^{3+}, and the remaining two peaks are attributed to oscillatory satellite peaks [44,45]. It should be noted that the peak density of Fe^{3+} for S-NiFe LDH-10 was much stronger than that for S-NiFe LDH-2, S-NiFe LDH-5 and S-NiFe LDH-20, suggesting that as the concentration of the sulfur source increased, the production of NiFe LDH increased, but an excessive sulfur source concentration also resulted in an inhibition of Fe^{3+} formation. As a result, the atomic percentage of Ni to Ni + Fe in the catalyst gradually increased (29%, 55%, 60%, 81%) with the increase in Ni^{2+} concentration from 2 mmol to 20 mmol (Figure S3), while the atomic percentage of Fe correspondingly decreased (71%, 45%, 40%, 19%). It is speculated

that an increasing amount of Ni^{2+} will inhibit the reaction of Fe and then influence the electrocatalytic performance. The fitted high-resolution O 1s spectra (Figure S4) showed obvious peaks at binding energies of 529.0, 530.5 and 532.2 eV, representing M-O bonds, M-OH bonds and H_2O, respectively [46,47]. As for the S 2p spectrum, weak peak density can be clarified in the four samples (Figure S5a–d), indicating the successful doping of S on the surface of NiFe LDH [14]. The addition of sulfur sources plays three main roles: (i) promoting the surface corrosion on IF substrate; (ii) accelerating the formation of NiFe LDH; (iii) resulting in a S dopant in NiFe LDH structure. Therefore, the S-NiFe LDH with an optimized electronic structure and morphology is beneficial for improving the OER performance, especially the reaction activities and the reaction kinetics.
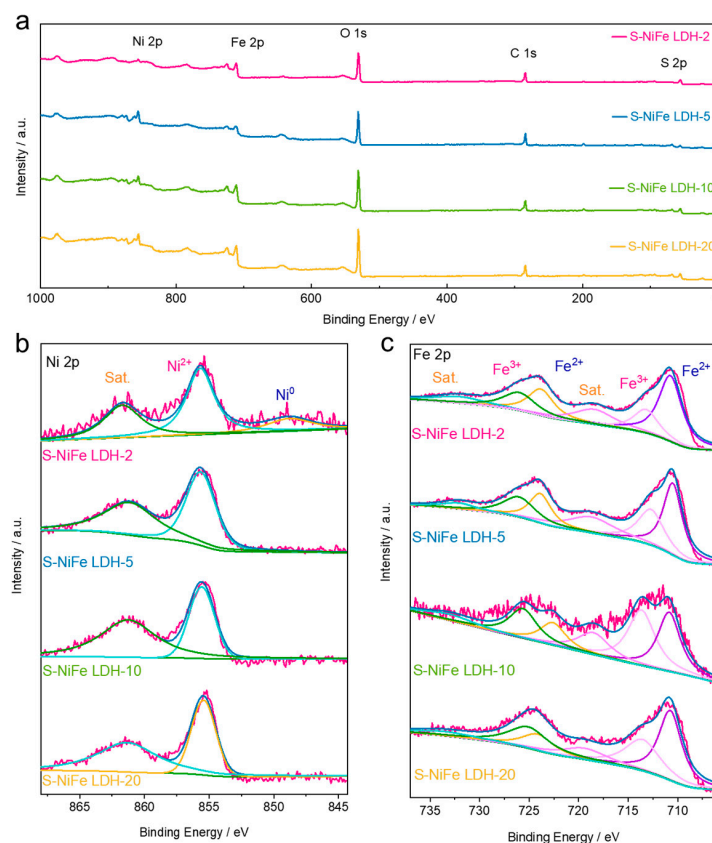

Figure 4. (**a**) XPS survey spectra of S-NiFe LDH-2, S-NiFe LDH-5, S-NiFe LDH-10 and S-NiFe LDH-20; (**b**) high-resolution XPS spectra of Ni 2p and (**c**) high-resolution XPS spectra of Fe 2p for the S-NiFe LDH-2, S-NiFe LDH-5, S-NiFe LDH and S-NiFe LDH-20 catalysts.

2.2. Electrochemical Performance

A three-electrode configuration was adopted to study the electrochemical OER properties. CV curves with a wide potential window were applied to explore the electrochemical process of the as-prepared catalysts. As shown in Figure 5a, the S-NiFe LDH-2, S-NiFe LDH-5, S-NiFe LDH-10 and S-NiFe LDH-20 showed distinct redox peaks, in which the oxidation peak of S-NiFe LDH-10 at approximately 0.40 V corresponds to the valence transition of Fe(II)/Fe(III) [48]. A much higher reduction peak current density of S-NiFe LDH-10 can be seen at a potential of approximately 1.0 V relative to the other three S-NiFe LDH catalysts, which corresponds to the valence transition process of Ni(II)/Ni(III) [49]. It should be noted that the oxidation peaks of the S-NiFe LDH catalysts were difficult to clarify and may be overlapped by the OER current. The surface valence transition may optimize the surface properties of the catalysts, which is beneficial for promoting the OER performance. Notably, the peak current density of S-NiFe LDH was significantly higher than that of the other three catalysts, indicating the presence of a rich electrochemical inter-

face. Subsequent linear scanning voltammetry (LSV) was conducted, and all four catalysts exhibited higher OER activity than commercial RuO_2 (Figure 5b). Moreover, S-NiFe LDH-10 has much superior OER activity compared to S-NiFe LDH-2, S-NiFe LDH-5, S-NiFe LDH-20 and IF (Figure S6a). To accurately measure OER activity, a histogram of the five catalysts (Figure 5c) at a current density of 10 mA cm^{-2} was drawn from polarization curves (Figure 5b). The overpotential of S-NiFe LDH-10 was only 120.0 mV, much smaller than that of S-NiFe LDH-2 (130.0 mV), S-NiFe LDH-5 (150.0 mV), S-NiFe LDH-20 (128.0 mV) and RuO_2 (310.0 mV). Tafel plots derived from the polarization curves in Figure 5b are shown in Figure 5d. The corresponding Tafel slopes were calculated to be 63.2 mV dec^{-1}, 61.8 mV dec^{-1}, 39.5 mV dec^{-1}, 61.2 mV dec^{-1} and 30.9 mV dec^{-1} for S-NiFe LDH-2, S-NiFe LDH-5, S-NiFe LDH-10, S-NiFe LDH-20 and RuO_2/IF, respectively. According to the Tafel slope values, S-NiFe LDH-10 corresponds to the Tafel process, and S-NiFe LDH-2, S-NiFe LDH-5 and S-NiFe LDH-20 follow a Volmer process [50]. The small Tafel slope value of S-NiFe LDH suggested a faster OER kinetics. Moreover, the OER activities of the catalysts obtained with different reaction times were also studied. It can be seen from Figure S6 that the catalysts synthesized at 6 h (NiFe LDH) have better OER activity than those prepared at other times.
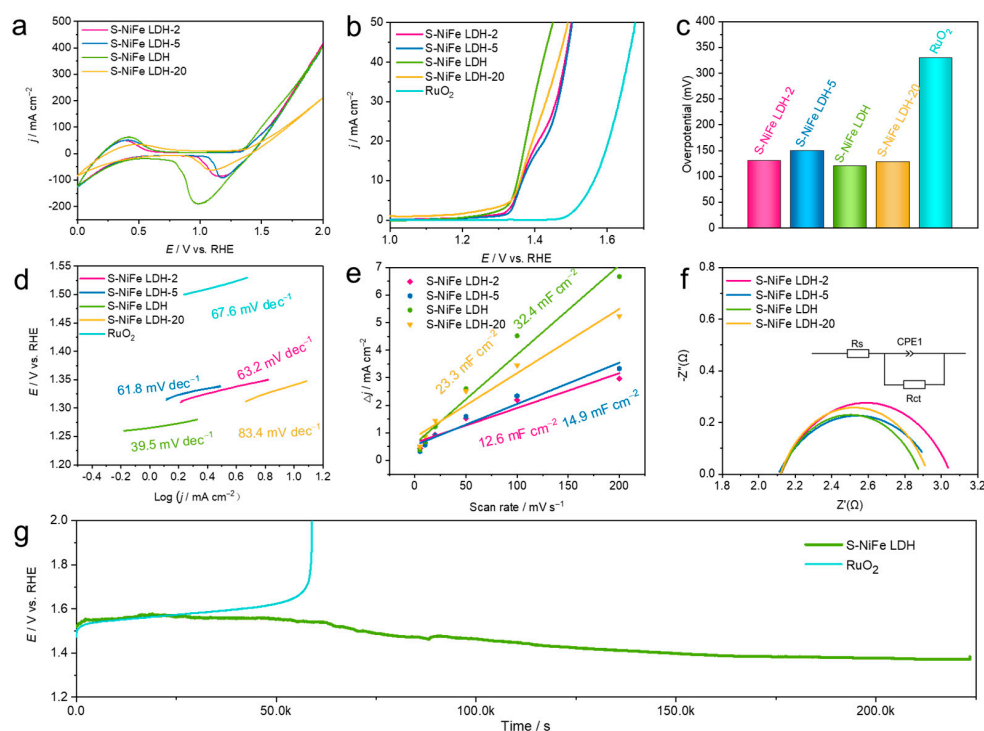

Figure 5. (**a**) CV curves of S-NiFe LDH catalysts with a potential window of 0.0–2.0 V vs. RHE; (**b**) OER polarization curves of the S-NiFe LDH catalysts and RuO_2/IF; (**c**) corresponding histograms at a current density of 10 mA cm^{-2} from (**b**); (**d**) corresponding Tafel plots derived from (**b**); (**e**) corresponding linear plots of the scan rates versus current density variation at 0.55 V for the S-NiFe LDH catalysts; (**f**) EIS spectrum of S-NiFe LDH catalysts with different Ni^{2+} concentrations and the equivalent circuit (inset); (**g**) chronopotentiometry test of S-NiFe LDH and RuO_2 at a constant current density of 10 mA cm^{-2}.

Considering that electrochemical activity surface area (ECSA) is a key parameter for determining the activity and kinetics of catalysts and taking account of the principle that the electrical double-layer capacitor (C_{dl}) is proportional to the ECSA, the C_{dl} values were calculated by measuring the CV curves at different scanning rates of the catalysts at a nonpseudocapacitance potential window of 0.5–0.6 V. As shown in Figure 5e and Figures S7–S10, the C_{dl} values of S-NiFe LDH-2, S-NiFe LDH-5, S-NiFe LDH-10 and S-NiFe LDH-20 were 6.3, 7.5, 16.2 and 11.6 mF cm^{-2}, respectively, demonstrating the excellent

electrochemical kinetics of S-NiFe LDH for the OER by exposing abundant electrochemical interfaces. The intrinsic electrical conductivity of the catalysts also plays a significant role in affecting the OER performance. As shown in Figure 5f, the S-NiFe LDH showed the smallest semicircle diameter compared to the other three catalysts, demonstrating the excellent electrical conductivity properties of S-NiFe LDH. Moreover, the catalysts obtained at different reaction times also demonstrated excellent conductivity with a corrosion time of 6 h (Figure S11 and Table S3).

Electrochemical stability is also significant for practical water-splitting applications. Therefore, the electrochemical stability of S-NiFe LDH and commercial RuO_2 catalysts was tested via the chronopotentiometry strategy at a constant current density of 10 mA cm^{-2}. It can be seen from Figure 5g that S-NiFe LDH showed excellent stability after continuous working of 250 ks (~68 h). It should be noted that the potential showed an obvious decreasing tendency from ~70 ks to 150 ks, which may be ascribed to the activation of the S-NiFe LDH at the surface of the catalyst. In contrast, the potential of the RuO_2 catalyst gradually increased and failed at 60 ks (~17 h), indicating the excellent electrochemical stability of S-NiFe LDH for the OER. The structural integrity of the S-NiFe LDH was characterized by Raman spectroscopy, SEM and corresponding EDS maps after a stability test. As shown from the Raman spectroscopy of Figure 6a, although the relative intensity of S-NiFe LDH decreased after the stability test compared to the pristine S-NiFe LDH, the main composition showed negligible change, demonstrating the excellent electrochemical stability of S-NiFe LDH. In addition, the ultra-thin lamellar assembled morphology was still maintained after a ~68 h stability test demonstrated, as demonstrated by an SEM image (Figure 6b) with typical EDS spectra peaks (Figure 6c). The enlarged magnification of the SEM image and corresponding EDS maps demonstrated a uniform distribution of Fe and O but an inverse distribution of Ni and S, demonstrating a surface reconstruction of Ni and Fe species, in which the Ni and S were covered by the Fe and O after the stability test.
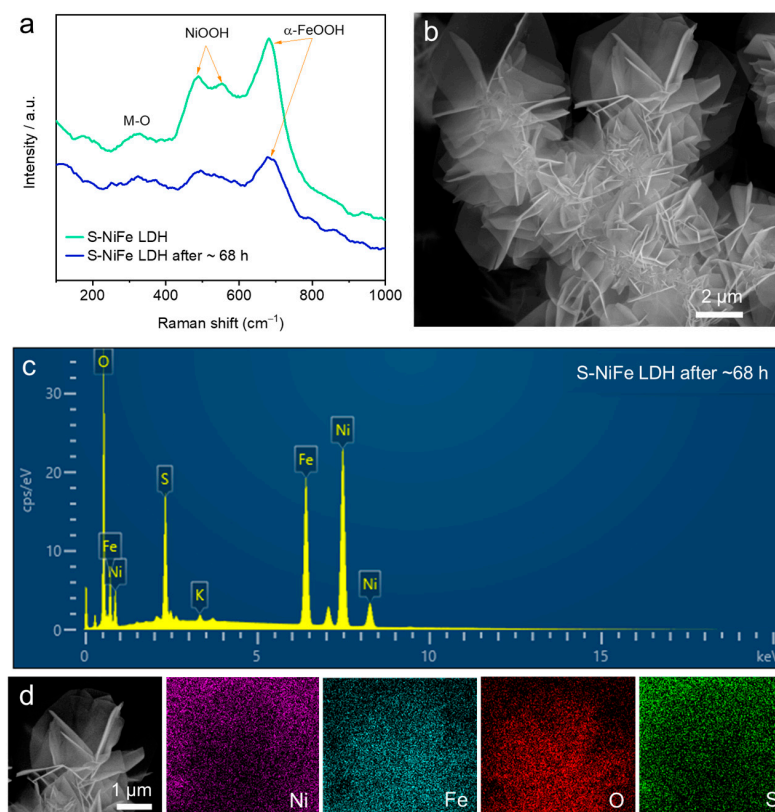

Figure 6. (**a**) Raman spectroscopy of S-NiFe LDH before and after stability tests; SEM image (**b**) and EDS spectrum (**c**) of S-NiFe LDH after stability test; (**d**) SEM image and corresponding EDS maps of S-NiFe LDH after stability test.

3. Materials and Methods

3.1. Materials and Agents

IF was bought from Cyber Electrochemical Materials Network Co., Ltd. (Tokyo, Japan), with a thickness of 1 mm; HCl and ethanol were purchased from Sinopharm Chemical Re-agent Co., Ltd. (Shanghai, China), at analytical grade; RuO_2 was purchased from Shanghai Maclin Bio-chemical Technology Co., Ltd. (Shanghai, China), at ≥99.9% grade; $NiCl_2$ $6H_2O$ was purchased from Aladdin Chemical Reagent Co., Ltd. (Shanghai, China), at ≥98% grade, and used without further purification; KOH and $Na_2S_2O_3$ were purchased from Sinopharm Chemical Reagent Co., Ltd. (Shanghai, China), at analytical grade.

3.2. Preparation of Sulfur-Doped NiFe LDH Catalysts

The IF substrate was initially cut into a size of 2×2 cm and then submerged in a beaker containing 0.1 M HCl solution for 10 min to eliminate surface impurities. Following this step, the IF was rinsed three times, alternating between deionized water and ethanol, to ensure thorough cleaning. Subsequently, the cleaned IF was dried in a vacuum oven at 60 °C.

A fast room-temperature corrosion engineering strategy was employed for the synthesis of S-NiFe LDH. In detail, 10 mmol of $NiCl_2$ $6H_2O$ and 0.3 mmol of $Na_2S_2O_3$ were dissolved in a beaker containing 10 mL of deionized water under continuous magnetic stirring. The prepared IF substrate was then immersed in this solution and allowed to react for 6 h at room temperature. After the reaction period, the IF substrate was carefully removed from the solution and washed repeatedly with deionized water and ethanol alternately to remove any residual chemicals or byproducts. Finally, the washed substrate was dried at 60 °C for 10 h to obtain the desired S-NiFe LDH material.

To study the effect of etching time on the physical properties of the S-NiFe LDH catalysts, the reaction time was controlled to 2 h, 4 h, 6 h, 8 h and 10 h, and the corresponding resulting catalysts were denoted as S-NiFe LDH-2h, S-NiFe LDH-4h, S-NiFe LDH-6h, S-NiFe LDH-8h and S-NiFe LDH-10h, respectively. Moreover, to study the concentration effect of metal salt, the reaction was carried out with Ni^{2+} concentrations of 2 mmol, 5 mmol, 10 mmol and 20 mmol, and the corresponding resulting catalysts were denoted as S-NiFe LDH-2, S-NiFe LDH-5, S-NiFe LDH-10 and S-NiFe LDH-20, respectively. Notably, the concentration of $Na_2S_2O_3$ was kept constant for the construction of different catalysts. According to the preparation steps, S-NiFe LDH-6h and S-NiFe LDH-10 refer to the same catalyst as S-NiFe LDH.

3.3. Material Characterization

XRD patterns were obtained via a TD-3700 instrument with Cu Kα radiation ($\lambda = 1.5406$ Å); the scanning speed was $8°$ min^{-1}. Scanning electron microscopy (SEM (Tokyo, Japan), JSM-IT500) was adopted to characterize the morphology and microstructure evolution of the as-prepared catalysts. Transmission electron microscopy (TEM, JEOL (Tokyo, Japan) JEM-2100F) was adopted to characterize the microstructure of the prepared catalysts. X-ray photoelectron spectroscopy (XPS (Falconbridge, ON, Canada), Axis-Ultra DLD-600W) was adopted to analyze the surface properties of the catalysts. Raman spectroscopy was performed using a Raman spectrometer (DXR (Carbondale, IL, USA) 2xi Raman microscope with excitation laser beam wavelength of 532.17 nm).

3.4. Electrochemical Measurements

All electrochemical tests were conducted using a three-electrode system with a CHI 660E electrochemical workstation (CH instruments). In this setup, a 1 M KOH solution served as the electrolyte, a graphite rod acted as the counter electrode, a reversible hydrogen electrode (RHE) functioned as the reference electrode, and the catalyst-loaded IF was employed as the working electrode with an impregnation area of 1 cm^2, and the electrochemical results were normalized to the surface area, which was assumed to be 1×1 cm = 1 cm^2. Cyclic voltammetry (CV) measurements were performed to assess the

electrochemical properties of the catalyst. The scanning rate was set at 50 mV s^{-1} with a potential window ranging from 0 to 2.0 V. To determine the double-layer capacitance (C_{dl}), CV measurements were carried out within a nonpseudocapacitance potential window of 0.5 to 0.6 V, and the scanning rate was varied from 10 mV s^{-1} to 200 mV s^{-1}. For linear scanning voltammetry (LSV), the potential window was set between 0.8 and 1.8 V, with a scanning rate of 5 mV s^{-1}. EIS was performed at a potential of 1.5 V (vs. RHE); the rate ranged from 0.01 to 100,000 Hz, and the amplitude values were set to 5 mV. The EIS spectra were interpreted by fitting them to equivalent circuits.

For comparison, the RuO_2 catalyst was prepared by weighing 5 mg of RuO_2, dispersing it into 1 mL of a 0.1% concentration Nafion/iso-propyl alcohol solution, and subjecting the mixture to ultrasonication for 15 min. Then, 100 μL of the dispersion was taken, added to the surface of the IF substrate drop by drop, and dried naturally.

4. Conclusions

In summary, we have successfully synthesized a S-NiFe LDH with an ultra-thin lamellar self-assembled microsphere structure directly on an IF substrate using a rapid room-temperature corrosion engineering strategy. This innovative approach allowed us to tailor the yield of the NiFe LDH by precisely adjusting the amount of Ni^{2+} and the reaction time. The introduction of sulfur sources in the corrosion medium played a pivotal role in three main aspects: Firstly, it facilitated the surface corrosion of the IF substrate, creating an ideal foundation for the subsequent deposition of the NiFe LDH. Secondly, it accelerated the formation of the NiFe LDH phase. Lastly, the sulfur sources acted as dopants within the NiFe LDH structure, enhancing its catalytic properties. The resulting S-NiFe LDH, with its 3D microsphere structure and sulfur dopants, exhibited exceptional performance for the OER. Notably, the S-NiFe LDH catalyst demonstrated remarkable activity with an overpotential of 120.0 mV at a current density of 10 mV cm^{-2}, showcasing its efficiency in initiating the OER process. Such activity also outperformed most of the recently published OER catalysts (Table S4). Additionally, the catalyst displayed favorable reaction kinetics, as indicated by a Tafel slope of 39.5 mV dec^{-1} and a double-layer capacitance (C_{dl}) value of 31.3 mF cm^{-2}. These results highlight the effectiveness of our expedited NiFe LDH construction strategy in producing a high-performance OER catalyst. Consequently, further investigation into optimizing the S-NiFe LDH catalyst will involve precisely controlling the sulfur doping levels to enhance the OER performance. Additionally, we plan to implement a practical water-splitting setup to evaluate the high-current production of hydrogen and oxygen, utilizing the S-NiFe LDH catalyst as the anode, in order to fulfill the needs of the green hydrogen industry.

Author Contributions: Conceptualization, J.W., X.Z. and J.Z.; methodology, J.W.; software, Y.M.; validation, J.W., Y.M. and J.Z.; formal analysis, J.W.; investigation, Y.M., H.L., L.W. and C.S.; resources, J.W. and L.G.; data curation, Y.M. and J.W.; writing—original draft preparation, Y.M.; writing—review and editing, J.W. and J.Z.; visualization, J.Z.; supervision, J.W., X.Z. and J.Z.; project administration, J.W.; funding acquisition, J.Z. All authors have read and agreed to the published version of the manuscript.

Data Availability Statement: Original data can be obtained from the corresponding authors.

Conflicts of Interest: The authors declare no conflicts of interest.

References

1. Yoro, K.O.; Daramola, M.O. CO_2 emission sources, greenhouse gases, and the global warming effect. Advances in carbon capture. In *Advances in Carbon Capture*; Woodhead Publishing: Sawston, UK, 2020; pp. 3–28.

2. Shahsavari, A.; Akbari, M. Potential of solar energy in developing countries for reducing energy-related emissions. *Renew. Sustain. Energy Rev.* **2018**, *90*, 275–291. [CrossRef]

3. Zou, X.; Liu, Y.P.; Li, G.D.; Wu, Y.Y.; Liu, D.P.; Li, W.; Li, H.W.; Wang, D.J.; Zhang, Y.; Zou, X.X. Ultrafast Formation of Amorphous Bimetallic Hydroxide Films on 3D Conductive Sulfide Nanoarrays for Large-Current-Density Oxygen Evolution Electrocatalysis. *Adv. Mater.* **2017**, *29*, 1700404. [CrossRef] [PubMed]

4. Dong, B.; Xie, J.Y.; Wang, N.; Gao, W.K.; Ma, Y.; Chen, T.S.; Yan, X.T.; Li, Q.Z.; Zhou, Y.L.; Chai, Y.M. Zinc ion induced three-dimensional Co_9S_8 nano-neuron network for efficient hydrogen evolution. *Renew. Energy* **2020**, *157*, 415–423. [CrossRef]

5. Ding, Y.; Miao, B.Q.; Li, S.N.; Jiang, Y.C.; Liu, Y.Y.; Yao, H.C.; Chen, Y. Benzylamine oxidation boosted electrochemical water-splitting: Hydrogen and benzonitrile co-production at ultra-thin Ni_2P nanomeshes grown on nickel foam. *Appl. Catal. B Environ.* **2020**, *268*, 118393. [CrossRef]

6. Zhang, R.R.; Wang, L.; Pan, L.; Chen, Z.C.; Jia, W.Y.; Zhang, X.W.; Zou, J.J. Solid-acid-mediated electronic structure regulation of electrocatalysts and scaling relation breaking of oxygen evolution reaction. *Appl. Catal. B Environ.* **2020**, *277*, 119237. [CrossRef]

7. Zhang, J.Y.; Yan, Y.; Mei, B.B.; Qi, R.J.; He, T.; Wang, Z.T.; Fang, W.S.; Zaman, S.D.; Su, Y.Q.; Ding, S.J.; et al. Local spin-state tuning of cobalt–iron selenide nanoframes for the boosted oxygen evolution. *Energy Environ. Sci.* **2021**, *14*, 365–373. [CrossRef]

8. Ma, T.F.; Xu, W.W.; Li, B.R.; Chen, X.; Zhao, J.J.; Wan, S.S.; Jiang, K.; Zhang, S.X.; Wang, Z.F.; Tian, Z.Y.; et al. The Critical Role of Additive Sulfate for Stable Alkaline Seawater Oxidation on Nickel-Based Electrodes. *Angew. Chem. Int. Ed.* **2021**, *60*, 22740–22926. [CrossRef] [PubMed]

9. Guo, F.F.; Wu, Y.Y.; Chen, H.; Liu, Y.P.; Yang, L.; Ai, X.; Zou, X.X. High-performance oxygen evolution electrocatalysis by boronized metal sheets with self-functionalized surfaces. *Energy Environ. Sci.* **2019**, *12*, 684–692. [CrossRef]

10. Wang, B.; Tang, C.; Wang, H.F.; Chen, X.; Cao, R.; Zhang, Q. A Nanosized CoNi Hydroxide@Hydroxysulfide Core–Shell Heterostructure for Enhanced Oxygen Evolution. *Adv. Mater.* **2018**, *31*, 1805658. [CrossRef]

11. Yang, H.; Gong, L.Q.; Wang, H.M.; Dong, C.L.; Wang, J.L.; Qi, K.; Liu, H.F.; Guo, X.P.; Xia, B.Y. Preparation of nickel-iron hydroxides by microorganism corrosion for efficient oxygen evolution. *Nat. Commun.* **2020**, *11*, 5075. [CrossRef]

12. Tang, Y.H.; Liu, Q.; Dong, L.; Wu, H.B.; Yu, X.Y. Activating the hydrogen evolution and overall water splitting performance of NiFe LDH by cation doping and plasma reduction. *Appl. Catal. B Environ.* **2020**, *266*, 118627. [CrossRef]

13. Zhang, X.Y.; Li, F.T.; Dong, Y.W.; Dong, B.; Dai, F.N.; Liu, C.G.; Chai, Y.M. Dynamic anion regulation to construct S-doped FeOOH realizing 1000 $mAcm^{-2}$-level-current-density oxygen evolution over 1000 h. *Appl. Catal. B Environ.* **2022**, *315*, 121571. [CrossRef]

14. Rao, R.R.; Stephens, I.E.L.; Durrant, J.R. Understanding What Controls the Rate of Electrochemical Oxygen Evolution. *Joule* **2021**, *5*, 16–18. [CrossRef]

15. Yuan, W.Y.; Wang, S.Y.; Ma, Y.Y.; Qiu, Y.; An, Y.R.; Cheng, L.F. Interfacial Engineering of Cobalt Nitrides and Mesoporous Nitrogen-Doped Carbon: Toward Efficient Overall Water-Splitting Activity with Enhanced Charge-Transfer Efficiency. *ACS Energy Lett.* **2020**, *5*, 692–700. [CrossRef]

16. Zhang, R.; Wang, X.X.; Yu, S.J.; Wen, T.; Zhu, X.W.; Yang, F.X.; Sun, X.N.; Wang, X.K.; Hu, W.P. Ternary $NiCo2Px$Nanowires as pH-Universal Electrocatalysts for Highly Efficient Hydrogen Evolution Reaction. *Adv. Mater.* **2016**, *29*, 1605502. [CrossRef]

17. Zhang, J.; Cui, R.J.; Gao, C.C.; Bian, L.Y.; Pu, Y.; Zhu, X.B.; Li, X.A.; Huang, W. Cation-Modulated HER and OER Activities of Hierarchical VOOH Hollow Architectures for High-Efficiency and Stable Overall Water Splitting. *Small* **2019**, *15*, 1904688. [CrossRef]

18. Riyajuddin, S.; Tarik Aziz, S.K.; Kumar, S.; Nessim, G.D.; Ghosh, K. 3D-Graphene Decorated with g-C_3N_4/Cu_3P Composite: A Noble Metal-free Bifunctional Electrocatalyst for Overall Water Splitting. *ChemCatChem* **2020**, *12*, 1394–1402. [CrossRef]

19. Yue, S.; Wang, S.S.; Jiao, Q.Z.; Feng, X.T.; Zhan, K.; Dai, Y.Q.; Feng, C.H.; Li, H.S.; Feng, T.Y.; Zhao, Y. Preparation of Yolk–Shell-Structured $Co_xFe_{1−x}P$ with Enhanced OER Performance. *ChemSusChem* **2019**, *12*, 4461–4470. [CrossRef]

20. Yu, Z.Y.; Duan, Y.; Feng, X.Y.; Yu, X.X.; Gao, M.R.; Yu, S.H. Clean and Affordable Hydrogen Fuel from Alkaline Water Splitting: Past, Recent Progress, and Future Prospects. *Adv. Mater.* **2021**, *33*, 2007100. [CrossRef]

21. Wang, H.M.; Chen, S. A Cluster-Type Self-Healing Catalyst for Stable Saline–Alkali Water Splitting. *Catalysts* **2024**, *14*, 81. [CrossRef]

22. Zhao, Y.G.; Dongfang, N.C.; Triana, C.A.; Huang, C.; Erni, R.; Wan, W.C.; Li, J.; Stoian, D.; Pan, L.; Zhang, P.; et al. Dynamics and control of active sites in hierarchically nanostructured cobalt phosphide/chalcogenide-based electrocatalysts for water splitting. *Energy Environ. Sci.* **2022**, *15*, 727–739. [CrossRef]

23. Zhu, S.H.; Liu, T.T.; Yu, S.; Yang, H.J.; Sun, Q.M.; Zheng, J.Y. Constructing Stable MoO_x-NiS_x Film via Electrodeposition and Hydrothermal Method for Water Splitting. *Catalysts* **2023**, *13*, 1426. [CrossRef]

24. Ma, Y.J.; Wang, L.; Wang, J.; Sun, C.H.; Ma, C.L. In Situ Construction of Cobalt-Doped High-Dispersive Heazlewoodite for Efficient Oxygen Evolution. *Energy Fuels* **2023**, *37*, 5441–5447. [CrossRef]

25. Yan, B.; Krishnamurthy, D.; Hendon, C.H.; Deshpande, S.; Surendranath, Y.; Viswanathan, V. Surface Restructuring of Nickel Sulfide Generates Optimally Coordinated Active Sites for Oxygen Reduction Catalysis. *Joule* **2017**, *1*, 600–612. [CrossRef]

26. Hung, T.F.; Yin, Z.W.; Betzler, S.B.; Zheng, W.J.; Yang, J.W.; Zheng, H.M. Nickel sulfide nanostructures prepared by laser irradiation for efficient electrocatalytic hydrogen evolution reaction and supercapacitors. *Chem. Eng. J.* **2019**, *367*, 115–122. [CrossRef]

27. Wang, M.M.; Lin, M.T.; Li, J.T.; Huang, L.; Zhuang, Z.C.; Lin, C.; Zhou, L.; Mai, L.Q. Metal–organic framework derived carbon-confined Ni_2P nanocrystals supported on graphene for an efficient oxygen evolution reaction. *Chem. Commun.* **2017**, *53*, 8372–8375. [CrossRef]

28. Yang, Y.; Zeng, R.; Xiong, Y.; DiSalvo, F.J.; Abruña, H.D. Cobalt-Based Nitride-Core Oxide-Shell Oxygen Reduction Electrocatalysts. *J. Am. Chem. Soc.* **2019**, *141*, 19241–19245. [CrossRef]

29. Fan, Y.C.; Ida, S.; Staykov, A.; Akbay, T.; Hagiwara, H.; Matsuda, J.; Kaneko, K.; Ishihara, T. Ni-Fe Nitride Nanoplates on Nitrogen-Doped Graphene as a Synergistic Catalyst for Reversible Oxygen Evolution Reaction and Rechargeable Zn-Air Battery. *Small* **2017**, *13*, 1700099. [CrossRef]

30. Wang, X.; Li, Q.X.; Shi, P.H.; Fan, J.C.; Min, Y.L.; Xu, Q.J. Nickel Nitride Particles Supported on 2D Activated Graphene–Black Phosphorus Heterostructure: An Efficient Electrocatalyst for the Oxygen Evolution Reaction. *Small* **2019**, *15*, 1901530. [CrossRef]

31. Ibraheem, S.; Chen, S.G.; Li, J.; Wang, Q.M.; Wei, Z.D. In situ growth of vertically aligned FeCoOOH-nanosheets/nanoflowers on Fe,N co-doped 3D-porous carbon as efficient bifunctional electrocatalysts for rechargeable zinc–O_2 batteries. *J. Mater. Chem. A* **2019**, *7*, 9497–9502. [CrossRef]

32. Zang, N.; Wu, Z.X.; Wang, J.; Jin, W. Rational design of Cu–Co thiospinel ternary sheet arrays for highly efficient electrocatalytic water splitting. *J. Mater. Chem. A* **2020**, *8*, 1799–1807. [CrossRef]

33. Li, S.; Wan, J.X.; Liu, Z.Y.; Zhuang, M.D.; Ren, P.Y.; Shi, W.L.; Zeng, X.J.; Yang, J. Cyanogel-Based Preparation of Amorphous NiFe Nanoaggregates with Enhanced Activity and Stability for OER. *Catalysts* **2023**, *13*, 1261. [CrossRef]

34. Lin, J.; Ding, Y.H.; Jin, H.L.; Zeng, T.B. Optimized Ni, Co, Mn Oxides Anchored on Graphite Plates for Highly Efficient Overall Water Splitting. *Catalysts* **2023**, *13*, 1031. [CrossRef]

35. Anantharaj, S.; Kundu, S.; Noda, S. "The Fe Effect": A review unveiling the critical roles of Fe in enhancing OER activity of Ni and Co based catalysts. *Nano Energy* **2021**, *80*, 105514. [CrossRef]

36. Mohammed-Ibrahim, J. A review on NiFe-based electrocatalysts for efficient alkaline oxygen evolution reaction. *J. Power Sources* **2020**, *448*, 227375. [CrossRef]

37. Gao, R.; Yan, D.P. Recent Development of Ni/Fe-Based Micro/Nanostructures toward Photo/Electrochemical Water Oxidation. *Adv. Energy Mater.* **2019**, *10*, 1900954. [CrossRef]

38. Kang, B.K.; Hussain, M.B.; Cheng, X.X.; Peng, C.; Wang, Z.Q. Green electrodeposition synthesis of NiFe-LDH/MoO_x/$BiVO_4$ for efficient photoelectrochemical water splitting. *J. Colloid Interface Sci.* **2022**, *626*, 146–155. [CrossRef]

39. Ma, Y.M.; Wang, K.; Liu, D.U.; Yang, X.X.; Wu, H.; Xiao, C.H.; Ding, S.J. Surface dual-oxidation induced metallic copper doping into NiFe electrodes for electrocatalytic water oxidation. *J. Mater. Chem. A* **2019**, *7*, 22889. [CrossRef]

40. Li, X.G.; Liu, C.; Fang, Z.T.; Xu, L.; Lu, C.L.; Hou, W.H. Ultrafast Room-Temperature Synthesis of Self-Supported NiFe-Layered Double Hydroxide as Large-Current–Density Oxygen Evolution Electrocatalyst. *Small* **2021**, *18*, 2104354. [CrossRef]

41. Du, S.C.; Ren, Z.Y.; Wang, X.L.; Wu, J.; Meng, H.Y.; Fu, H.G. Controlled Atmosphere Corrosion Engineering toward Inhomogeneous NiFe-LDH for Energetic Oxygen Evolution. *ACS Nano* **2022**, *16*, 7794–7803. [CrossRef]

42. Wang, J.; Xu, J.X.; Guo, X.Y.; Shen, T.; Xuan, C.J.; Tian, B.L.; Wen, Z.R.; Zhu, Y.; Wang, D.L. Synergistic regulation of nickel doping/hierarchical structure in cobalt sulfide for high performance zinc-air battery. *Appl. Catal. B Environ.* **2021**, *298*, 120539. [CrossRef]

43. Wang, J.; Guo, X.Y.; Du, X.q.; Liang, J.n.; Wu, J.z.; Zhao, G.m.; Li, X.G.; Gui, S.W.; Zheng, F.Y.; Zhao, J.; et al. Revealing the complex lithiation pathways and kinetics of core-shell NiO@CuO electrode. *Energy Storage Mater.* **2022**, *51*, 11–18. [CrossRef]

44. Ren, Z.X.; Li, X.H.; Peng, Y.J.; Wang, G.Z.; Yin, J.; Zhao, X.C.; Wang, W.; Wang, X.B. $FeNiS_2$/reduced graphene oxide electrocatalysis with reconstruction to generate FeNi oxo/hydroxide as a highly-efficient water oxidation electrocatalyst. *Rare Met.* **2022**, *41*, 4127–4137. [CrossRef]

45. Chen, Y.F.; Li, J.H.; Liu, T.T.; You, S.H.; Liu, P.; Li, F.J.; Gao, M.Q.; Chen, S.G.; Zhang, F.F. Constructing robust NiFe LDHs–NiFe alloy gradient hybrid bifunctional catalyst for overall water splitting: One-step electrodeposition and surface reconstruction. *Rare Met.* **2023**, *42*, 2272–2283. [CrossRef]

46. Zhou, Y.N.; Yu, W.L.; Cao, Y.N.; Zhao, J.; Dong, B.; Ma, Y.; Wang, F.L.; Fan, R.Y.; Zhou, Y.L.; Chai, Y.M. S-doped nickel-iron hydroxides synthesized by room-temperature electrochemical activation for efficient oxygen evolution. *Appl. Catal. B-Environ* **2021**, *292*, 120150. [CrossRef]

47. Wang, W.; Wang, Z.X.; Hu, Y.C.; Liu, Y.C.; Chen, S.L. A potential-driven switch of activity promotion mode for the oxygen evolution reaction at Co_3O_4/NiO_xH_y interface. *eScience* **2022**, *2*, 438–444. [CrossRef]

48. Hao, M.; Wang, H.; Zhang, X.; Qu, Y.; Xuan, C.; Wu, Z.; Cui, M.; Wang, J. In situ construction of self-supporting Ni–Fe sulfide for high-efficiency oxygen evolution. *New J. Chem.* **2022**, *46*, 8250–8255. [CrossRef]

49. Wang, Y.; Tao, S.; Lin, H.; Han, S.; Zhong, W.; Xie, Y.; Hu, J.; Yang, S. $NaBH_4$ induces a high ratio of Ni^{3+}/Ni^{2+} boosting OER activity of the NiFe LDH electrocatalyst. *RSC Adv.* **2020**, *10*, 33475–33482. [CrossRef]

50. Samal, A.; Kori, D.K.K.; Jain, A.; Das, A.K. A nickel-doped two-dimensional covalent organic polymer (2D-COP) for electrocatalytic hydrogen evolution reaction. *ACS Appl. Energy Mater.* **2024**, *7*, 2715–2725. [CrossRef]

51. Zhou, C.H.; Chen, X.; Liu, S.; Han, Y.; Meng, H.B.; Jiang, Q.Y.; Zhao, S.M.; Wei, F.; Sun, J.; Tian, T.; et al. Superdurable Bifunctional Oxygen Electrocatalyst for HighPerformance Zinc–Air Batteries. *J. Am. Chem. Soc.* **2022**, *144*, 2694–2704. [CrossRef]

52. Gao, X.Y.; Chen, J.; Sun, X.Z.; Wu, B.F.; Li, B.; Ning, Z.C.; Li, J.; Wang, N. Ru/RuO_2 Nanoparticle Composites with N-Doped Reduced Graphene Oxide as Electrocatalysts for Hydrogen and Oxygen Evolution. *ACS Appl. Nano Mater.* **2020**, *3*, 12269–12277. [CrossRef]

53. Li, J.W.; Xu, W.M.; Zhou, D.; Luo, J.X.; Zhang, D.W.; Xu, P.M.; Wei, L.C.; Yuan, D.S. Synthesis of 3D flower-like cobalt nickel phosphate grown on Ni foam as an excellent electrocatalyst for the oxygen evolution reaction. *J. Mater. Sci.* **2018**, *53*, 2077–2086. [CrossRef]

54. Xu, J.C.; Li, Z.L.; Chen, D.; Yang, S.X.; Zheng, K.W.; Ruan, J.X.; Wu, Y.L.; Zhang, H.; Chen, J.; Xie, F.Y.; et al. Porous Indium Tin Oxide-Supported NiFe LDH as a Highly Active Electrocatalyst in the Oxygen Evolution Reaction and Flexible Zinc–Air Batteries. *ACS Appl. Mater. Interfaces* **2021**, *13*, 48774–48783. [CrossRef]

55. Lin, Y.P.; Wang, H.; Peng, C.K.; Bu, L.M.; Chiang, C.L.; Tian, K.; Zhao, Y.; Zhao, J.Q.; Lin, Y.G.; Lee, J.M.; et al. Co-Induced Electronic Optimization of Hierarchical NiFe LDH for Oxygen Evolution. *Small* **2021**, *16*, 2002426. [CrossRef]

56. Chen, J.S.; Ren, J.; Shalom, M.; Fellinger, T.; Antonietti, M. Stainless Steel Mesh-Supported NiS Nanosheet Array as Highly Efficient Catalyst for Oxygen Evolution Reaction. *ACS Appl. Mater. Interfaces* **2016**, *8*, 5509–5516. [CrossRef]

57. Gao, L.; Guo, C.; Liu, X.; Ma, X.; Zhao, M.; Kuang, X.; Yang, H.; Zhu, X.; Sun, X.; Wei, Q. Co-Doped FeS_2 with a porous structure for efficient electrocatalytic overall water splitting. *New J. Chem.* **2020**, *44*, 1711–1718. [CrossRef]

58. Wu, S.W.; Liu, S.Q.; Tan, X.H.; Zhang, W.Y.; Cadien, K.; Li, Z. Ni_3S_2-embedded NiFe LDH porous nanosheets with abundant heterointerfaces for high-current water electrolysis. *Chem. Eng. J.* **2022**, *442*, 136105. [CrossRef]

59. Zhao, M.H.; Wang, Y.N.; Mi, W.L.; Wu, J.T.; Zou, J.J.; Zhu, X.D.; Gao, J.; Zhang, Y.C. Surface-modified amorphous FeOOH on NiFe LDHs for high efficiency electrocatalytic oxygen evolution. *Electrochim. Acta* **2023**, *458*, 142513. [CrossRef]

60. Hu, L.Y.; Zeng, X.; Wei, X.Q.; Wang, H.J.; Wu, Y.; Gu, W.L.; Shi, L.; Zhu, C.Z. Interface engineering for enhancing electrocatalytic oxygen evolution of NiFe LDH/NiTe heterostructures. *Appl. Catal. B-Environ.* **2020**, *273*, 119014. [CrossRef]